ACS Photonics

pubs.acs.org/journal/apchd5

Letter

Inverse-Designed Narrowband THz Radiator for Ultrarelativistic Electrons

Benedikt Hermann,[#] Urs Haeusler,[#] Gyanendra Yadav, Adrian Kirchner, Thomas Feurer, Carsten Welsch, Peter Hommelhoff, and Rasmus Ischebeck*

Cite This: *ACS Photonics* 2022, 9, 1143−1149

Read Online

ACCESS | Metrics & More | Article Recommendations

ABSTRACT: THz radiation finds various applications in science and technology. Pump−probe experiments at free-electron lasers typically rely on THz radiation generated by optical rectification of ultrafast laser pulses in electro-optic crystals. A compact and cost-efficient alternative is offered by the Smith−Purcell effect: a charged particle beam passes a periodic structure and generates synchronous radiation. Here, we employ the technique of photonic inverse design to optimize a structure for Smith−Purcell radiation at a single wavelength from ultrarelativistic electrons. The resulting design is highly resonant and emits narrowbandly. Experiments with a 3D-printed model for a wavelength of 900 μm show coherent enhancement. The versatility of inverse design offers a simple adaption of the structure to other electron energies or radiation wavelengths. This approach could advance beam-based THz generation for a wide range of applications.

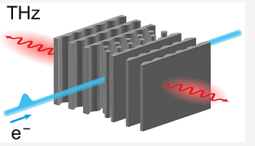

KEYWORDS: *THz generation, Smith−Purcell radiation, inverse design, light−matter interaction, free-electron light sources*

Sources of THz radiation are of interest for numerous applications, including wireless communication,[1,2] electron acceleration,[3−5] and biomedical and material science.[6,7] Free-electron laser (FEL) facilities demand versatile THz sources for pump−probe experiments.[8] Intense, broadband THz pulses up to sub-mJ pulse energy have been demonstrated using optical rectification of high-power femtosecond lasers in lithium niobate crystals.[9,10] The Smith−Purcell effect[11] offers a compact and cost-efficient alternative for the generation of beam-synchronous THz radiation at electron accelerators. This effect describes the emission of electromagnetic waves from a periodic metallic or dielectric structure excited by electrons moving parallel to its surface. The wavelength of Smith−Purcell radiation at an angle θ with respect to the electron beam follows:[11]

$$\lambda = \frac{a}{m}\left(\frac{1}{\beta} - \cos\theta\right) \tag{1}$$

where β is the normalized velocity of the electrons, a is the periodicity of the structure, and m is the mode order. Smith−Purcell emission from regular metallic grating surfaces has been observed in numerous experiments, first using 300 keV electrons[11] and later also using ultrarelativistic electrons.[12,13] If electron pulses shorter than the emitted wavelength are used, the fields from individual electrons add coherently, and the radiated energy scales quadratically with the bunch charge.[14] The typically used single-sided gratings emit a broadband spectrum,[15] which is dispersed by the Smith−Purcell relation (eq 1). To enhance emission at single frequencies, a concept called orotron uses a metallic mirror above the grating to form a resonator.[16,17] Dielectrics can sustain fields 1−2 orders of magnitude larger than metals[18] and are therefore an attractive material for strong Smith−Purcell interactions.

Inverse design is a computational technique that has been successfully employed to advance integrated photonics.[19] Algorithms to discover optical structures fulfilling desired functional characteristics are creating a plethora of novel subwavelength geometries: applications include wavelength-dependent beam splitters[19,20] and couplers,[21] as well as dielectric laser accelerators.[22]

RESULTS

The goal of our inverse design optimization was a narrowband dielectric Smith−Purcell radiator for ultrarelativistic electrons (E = 3.2 GeV, $\gamma \approx 6000$). To simplify the collection of the THz radiation, a periodicity of $a = \lambda$ was chosen, resulting in an emission perpendicular to the electron propagation direction, θ = 90°. The optimization was based on a 2D finite-difference frequency-domain (FDFD) simulation of a single unit cell of the grating (Figure 1a). Periodic boundaries in direction of the electron propagation ensure the desired periodicity, and perfectly matched layers in the transverse x-direction imitate free space. The design region extends 4.5 mm to each side of a 150 μm wide vacuum channel, large enough to facilitate the full transmission of the electron beam with a

Received: December 16, 2021
Published: March 16, 2022

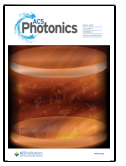

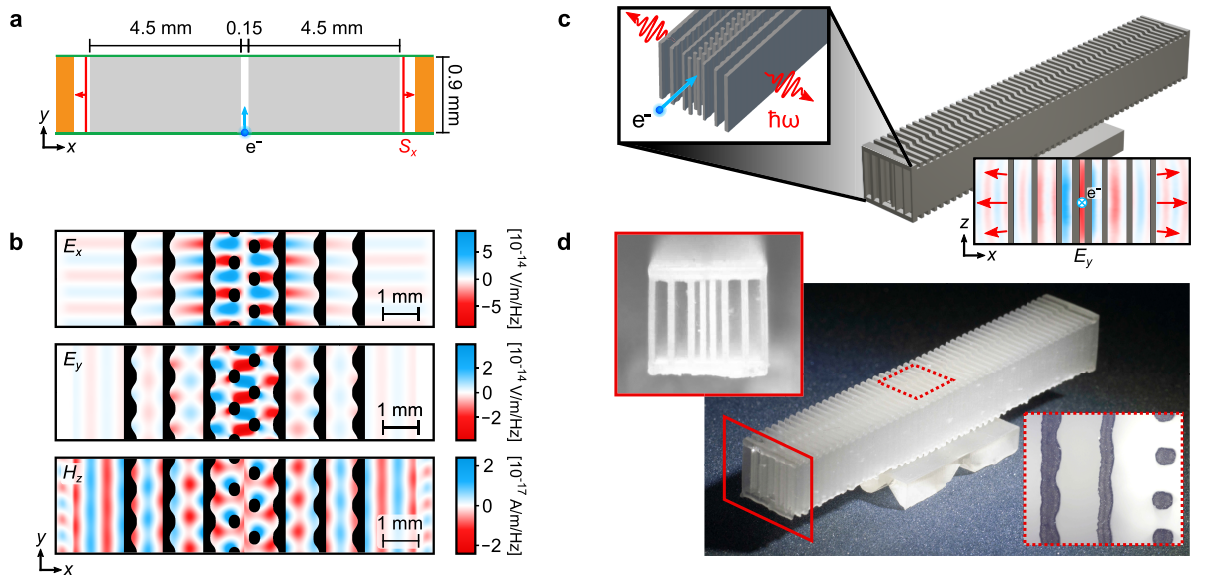

Figure 1. Inverse design and fabrication of THz radiator. (a) The design process is based on a 2D-FDFD simulation of a single unit cell of the grating (aspect ratio distorted). Applying periodic boundaries (green) in the longitudinal direction of the electron beam (blue) corresponds to the simulation of an infinitely long grating. In the transverse direction, we define perfectly matched layers (orange) to imitate free space. The design region (gray) extended 4.5 mm to each side of a 150 μm wide vacuum (white) channel for the electrons. The Poynting vector S_x was calculated outside the design region and served as the objective function of the optimization. (b) Optimized 2D design: structure material (black), vacuum (white), and associated electromagnetic field spectral density of the transverse-magnetic mode (red-blue). Three consecutive periods are shown. (c) 3D illustration of the extruded structure of (b) with 50 periods. The lower inset shows the electric field profile seen from the perspective of the electron obtained from a 3D-FDFD simulation. (d) Photograph of the inverse-designed structure fabricated by additive manufacturing. The dimensions of the entire structure are 6.5 × 6 × 45 mm (width × height × depth).

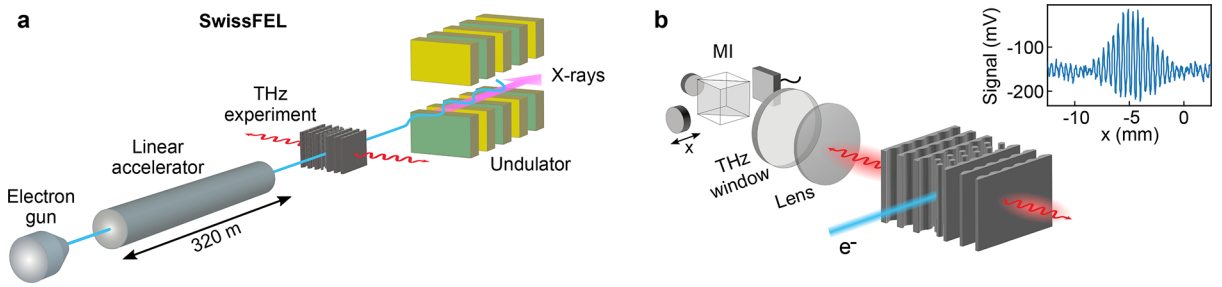

Figure 2. Experimental setup. (a) Schematic of SwissFEL. The THz generation experiments were conducted at the ACHIP interaction chamber[26] located in the switch-yard to the Athos beamline. (b) Sketch of the Smith−Purcell THz generation and Michelson interferometer (MI) setup. The inset shows a typical autocorrelation measurement.

width of σ_x = 30 μm (RMS). The electric current spectral density $\mathbf{J}(x, y, \omega)$ of a single electron bunch acts here as the source term of our simulation and is given by

$$\mathbf{J}(x, y, \omega) = \frac{q}{2\pi}\cdot(2\pi\sigma_x^2)^{-1/2}\cdot e^{-x^2/2\sigma_x^2}\cdot e^{-ik_y y}\hat{\mathbf{y}}$$

with the electron wavevector $k_y = 2\pi/\beta\lambda$ and the line charge density q. The absolute value of q is irrelevant for the optimization, but rough agreement with 3D simulations is found by choosing $q \sim Q/d$, where Q is the bunch charge and d the charge-structure distance.[23]

The optimization problem was to find a design (parametrized by the variable ϕ) that maximizes the radiation to both sides of the grating. Exploiting the full symmetry of the double-sided, perpendicular emission process, we enforced mirror and point symmetry with respect to the center of a unit cell of the grating. The design is defined by its relative permittivity $\varepsilon(x, y, \phi)$ and can only take the two values of vacuum, ε = 1, or the structure material, ε = 2.79. For simplicity, we neglected the small imaginary part ε'' = 0.08 of the material.[24]

The objective function G, quantifying the performance of a design ϕ, is given by the line integral of the Poynting vector $\mathbf{S}(x, y) = \mathrm{Re}\left\{\frac{1}{2}\mathbf{E}\times\mathbf{H}^*\right\}$ in the x-direction along the length of one period, evaluated at a point x_S outside the design region:

$$G(\phi) = \int_0^a S_x(x_S, y)\mathrm{d}y$$

The optimization problem can then be stated as

$$\max_\phi G(\phi) \quad \text{subject to} \quad \nabla\times\mathbf{E} = -i\omega\mu\mathbf{H} \quad \text{and}$$
$$\nabla\times\epsilon(\phi)^{-1}\nabla\times\mathbf{H} - \omega^2\mu\mathbf{H} = \nabla\times\epsilon(\phi)^{-1}\mathbf{J}$$

The design obtained from the gradient-based technique of adaptive moment estimation (Adam)[25] is depicted in Figure 1b. The structure features two rows of pillars, shifted by half a period with respect to each other. The rows of pillars are followed by three slabs on each side, which can be easily

https://doi.org/10.1021/acsphotonics.1c01932
ACS Photonics 2022, 9, 1143−1149

identified as distributed Bragg reflectors forming a microresonator around the electron channel. The channel width is 272 μm, even larger than the initially defined clearance of 150 μm. These slabs exhibit grooves, which perhaps act as a grating as well as a reflector. We note that these features are good examples of the superiority of inverse design over intuition-based designs.

To fabricate the geometry obtained with inverse design, we used an additive manufacturing process for poly(methyl methacrylate) (PMMA). A stereolithography device, featuring a resolution of 140 μm, is capable of reproducing the structure with subwavelength accuracy. The so-obtained structure is 6 mm high and 45 mm long (Figure 1d). The holder of the structure was manufactured together with the structure, and filaments connect the pillars and slabs on top of the structure for increased mechanical stability. We selected the Formlabs High Temperature Resin as a material for this study due to its excellent vacuum compatibility after curing in a heated vacuum chamber.[24] Afterward, the fabricated Smith–Purcell radiator was inserted into the ACHIP experimental chamber[26] at SwissFEL[27] (Figure 2a). The photoemitted electron bunch is accelerated to an energy of 3.2 GeV with the normal-conducting radio frequency accelerator at SwissFEL. A two-stage compression scheme using magnetic chicanes is employed to achieve an electron bunch length of approximately 30 fs at the interaction point. At this location, the transverse beam size was measured to be around 30 μm in the horizontal and 40 μm in the vertical direction.

An in-vacuum PMMA lens with a diameter of 25 mm collimated parts of the emitted radiation. A Michelson interferometer was used to measure the first-order autocorrelation of the electromagnetic pulse and to obtain its power spectrum via Fourier transform (Figure 2b and Methods). The measured spectrum is centered around 881 μm (0.34 THz) and has a full width at half-maximum of ~9% (Figure 3).

DISCUSSION

The observed spectrum agrees well with a 3D finite-differences time-domain (FDTD) simulation of the experiment (Figure 3). In contrast, a finite-differences frequency-domain (FDFD) simulation reveals that the design can in principal emit even more narrowbandly, originating from the high mode density inside the Fabry–Perot cavity formed by the two distributed Bragg reflectors on both sides of the electron channel. The difference between the two simulations can be explained by their distinct grid resolutions. The FDFD simulation considers only a single period of the structure with periodic boundaries, corresponding to an infinitely long structure. Hence, the cell size is small, allowing to use a high grid resolution. The time-domain simulation, on the other hand, calculates the electromagnetic field of the entire 50-period-long structure for each time step. This high memory requirement comes at the cost of a lower spatial resolution. Since the experiment was similarly limited by the fabrication resolution of 140 μm, the FDTD simulation reproduced the measured spectrum much better. We also note that potential absorption losses in the structure can reduce its quality factor and broaden the radiation spectrum. Due to the small contribution from $\varepsilon'' = 0.08$,[24] absorption effects were not considered here but would dominate at higher quality factors.

We drove the structure with electron bunches with a duration of approximately 30 fs (RMS), which is much shorter than the resonant wavelength corresponding to a period of 3 ps. Hence, we expect to see the coherent addition of radiated fields. To experimentally verify this, we varied the bunch charge. Figure 4 shows the detected pulse energy for six bunch charge settings ranging from 0 pC to 11.8 pC. The scaling is well approximated by a quadratic fit, which confirms the expected coherent enhancement of the THz pulse energy.[14] We observe a slight deviation for the highest charge measurement from the quadratic fit, which might be a result of detector saturation (see Methods). We note that the quadratic scaling would enable THz pulse energies orders of magnitude larger by driving the structure at higher bunch charges.

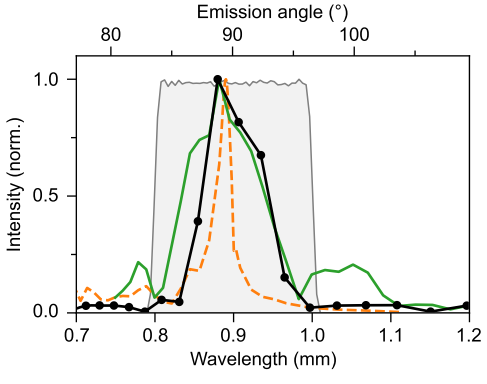

Figure 3. Emission spectra. The Fourier transform of an autocorrelation measurement with a Michelson interferometer (black) is compared to 3D time-domain (green) and frequency-domain (orange) simulations. The gray area indicates the acceptance window of the spectrometer, defined by the angular acceptance of the Michelson interferometer. The narrowness of emission originates from the high mode density inside the microresonator formed by the two distributed Bragg reflectors on each side of the electron channel.

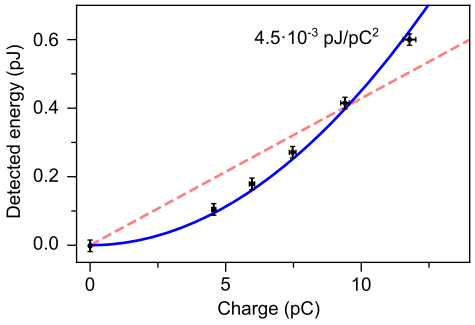

Figure 4. Coherent scaling. The detected pulse energy is shown as a function of the bunch charge. In contrast to the linear fit (dashed red), the quadratic fit (solid blue) approximates the measurements within the uncertainties, which confirms the expected coherent enhancement. Vertical and horizontal error bars represent the RMS detector noise obtained from a background measurement and the uncertainty in the charge measurement, respectively.

The THz pulse emitted perpendicular to the Smith-Purcell radiator possesses a pulse-front tilt of close to 45° since it is driven by ultrarelativistic electrons. Depending on the length of the radiator and the application, the tilt can be compensated for with a diffraction grating.

During and after our experiments, the structure did not show any signs of performance degradation or visible damage. It was

https://doi.org/10.1021/acsphotonics.1c01932
ACS Photonics 2022, 9, 1143–1149

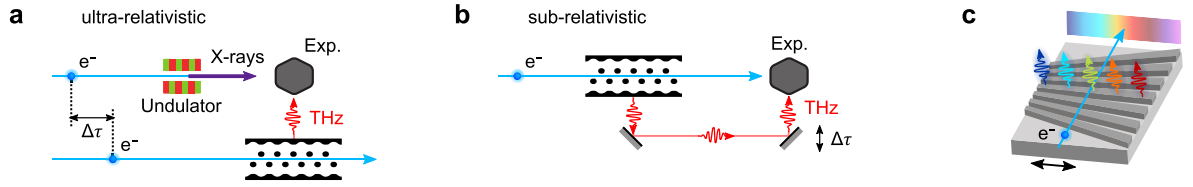

Figure 5. Possible applications of the beam-driven THz source in pump−probe experiments. (a) For ultrarelativistic electrons, a second electron bunch may be used to compensate for the longer path length of the THz pulse. X-rays are generated in the undulators of an FEL. (b) For subrelativistic electrons, the generated THz pulse is delayed to achieve simultaneous arrival of electron and THz radiation. (c) The structure becomes a tunable light source if the periodicity changes along the invariant direction; exemplified with a rectangular grating.

used continuously for eight hours with a bunch charge of approximately 10 pC at a pulse repetition rate of 1 Hz.

CONCLUSION

The here-presented beam-synchronous radiation source can be added to the beamline of an FEL to enrich capabilities for pump−probe experiments. For ultrarelativistic electrons, a second beamline may be used to compensate for the longer path length of the THz radiation and achieve simultaneous arrival with the X-ray radiation created in the undulator of the FEL (Figure 5a). Smith−Purcell radiation represents a cost-efficient alternative to the broadband generation of THz by optical rectification, which requires an external laser system and precise synchronization to the accelerator. Our inverse design approach to Smith−Purcell emitters can produce beam-synchronous narrowband THz radiation, which could propel pump−probe studies with THz excitations in solids, for instance, resonant control of strongly correlated electron systems, high-temperature superconductors, or vibrational modes of crystal lattices (phonons).[28,29]

Further improvement of our THz structure can be achieved by higher fabrication accuracy and the use of a fully 3D-optimized geometry with a higher quality factor, resulting in more narrowband emission and higher pulse energy. Moreover, the inverse design suite could be extended to composite structures of more than one material, which could provide extra stability for complicated 3D designs. In the case of highly resonant structures, materials with low absorption, for example, polytetrafluoroethylene (PTFE),[24] are a necessity. The measured THz pulse energy can be increased by a factor of almost 300 by raising the driving bunch charge from the used 11.8 pC up to the 200 pC available at SwissFEL. Whether the currently used material can withstand such high fields and radiation remains to be investigated. Combining 3D optimization, longer structures, larger collection optics, and higher bunch charges will result in a THz pulse energy multiple orders of magnitude larger than observed in the presented experiment (0.6 pJ).

Our work naturally extends to the field of subrelativistic electrons. Here, simultaneous arrival of THz radiation and electron bunches is readily achieved by compensating for the higher velocity of the radiation with a longer path length (Figure 5b). Besides its application for pump−probe experiments, our structure can be more generally applied as a radiation source at wavelengths that are otherwise difficult to generate. An advantage lies in the tunability that arises from changing the periodicity, either by replacing the entire structure or using a design with variable periodicity (Figure 5c), or from tuning the electron velocity. For the visible to UV regime, the idea of a compact device with the electron source integrated on a nanofabricated chip has recently sparked interest.[30,31]

METHODS

Structure Parametrization. Our inverse design process was carried out with an open-source Python package[32] suitable for 2D-FDFD gradient-based optimizations[25] of the chosen objective function $G(\phi)$ with respect to the design parameter ϕ. A key step lies in the parametrization of the structure $\varepsilon(\phi)$ through the variable ϕ in a way that ensures robust convergence of the algorithm and fabricability of the final design. In the most rudimentary case, $\varepsilon(x, y) = \phi(x, y)$ is a two-dimensional array with entries $\in [1, 2.79]$ for each pixel of the design area. Instead of setting bounds on the values of ϕ, we leave ϕ unbounded and apply a sigmoid function of the shape

$$\epsilon_r(x, y) = \epsilon_{\min} + (\epsilon_{\max} - \epsilon_{\min}) \cdot \frac{1}{2}(1 + \tanh \alpha\phi(x, y))$$

where large values of α yield a close-to-binary design with few values between $\varepsilon_{\min} = 1$ and $\varepsilon_{\max} = 2.79$. To avoid small or sharp features in the final design, we convolved $\phi(x, y)$ with a uniform 2D circular kernel with radius 60 μm before projection onto the sigmoid function $\tanh(\alpha\tilde{\phi})$ with the convolved design parameter $\tilde{\phi}$. By increasing α from 20 to 1000 as the optimization progresses, we found improved convergence. We further accelerated convergence by applying mirror and point symmetry with respect to the center of a unit cell of the grating, which reduces the parameter space by a factor of 4. An exemplary design evolution is shown in Figure 6.

Ultrarelativistic Optimization. The simulation of ultrarelativistic electrons poses challenges that have so far prevented inverse design in this regime.[33] Here, we report on two main challenges. First, the electron velocity is close to the speed of light ($\beta = 0.999999985$ for $E = 3.2$ GeV), which requires a high mesh resolution. If the numerical error is too large due to a low mesh resolution, the simulation may not be able to distinguish between $\beta < 1$ and $\beta > 1$. In that case, the simulation could show Cherenkov radiation in vacuum instead of Smith−Purcell radiation.

Not only does a higher mesh resolution require more computational memory and time, but it may also hamper the inverse design optimization if the number of design parameters becomes too large. Hence, we parametrized our structures at a low resolution (mesh spacing $\lambda/30$), which is still above the fabrication accuracy of $\lambda/5$, and computed the fields at a high resolution (mesh spacing $\lambda/150$).

The second difficulty arises from the long-range evanescent waves of ultrarelativistic electrons. The spectral density of the electric field of a line charge decays with $\exp(-\kappa|x|)$, where $\kappa = 2\pi/\beta\gamma\lambda$, with $\beta \approx 1$ and $\gamma \approx 6000$ for $E = 3.2$ GeV.[34] This

https://doi.org/10.1021/acsphotonics.1c01932
ACS Photonics 2022, 9, 1143−1149

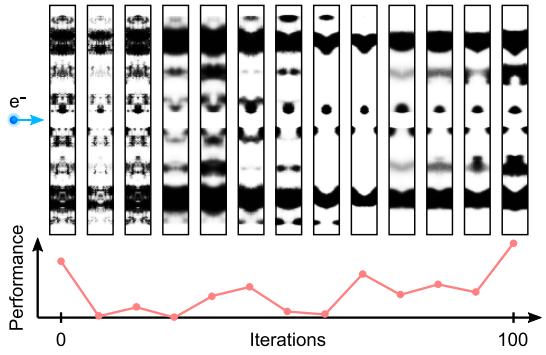

Figure 6. Exemplary design evolution. Left to right: The first 100 steps of an exemplary inverse design optimization are shown above their respective objective value in relative units. Starting from a random design, the design evolves under stochastic gradient-based optimization. At multiple steps throughout the optimization, the design solution is disturbed by the addition of random noise and blurring of features, which tests the stability of the design and helps in exploring a larger design space. Such a procedure was repeated ∼50×, each time yielding a different design depending on the initial randomized design (similar to particle swarm optimization). We then selected those design groups that gave best performance, stability, and fabricability (similar to supervised learning). Continuing the optimization from there and repetitively disturbing the solution, a final design will have gone through more than 1000 steps of optimization before fabrication. The displayed structure evolution used slightly different optimization conditions than the design presented in this work.

means the evanescent waves will reach the boundaries of our simulation cell in the x-direction. Generalized perfectly matched layers (PMLs)[35] are chosen, such that they can absorb both propagating and evanescent waves.

A detailed look at Figure 1b reveals that our implementation of generalized PMLs is not fully capable of absorbing evanescent waves. Hence, we make use of symmetry to further reduce the effect of evanescent waves at the boundaries of the simulation cell. Note that the evanescent electric field for $\beta \approx 1$ is almost entirely polarized along the transverse direction x. This means if the simulation cell is mirror symmetric with respect to the electron channel, antiperiodic boundaries can be applied after the PMLs to cancel out the effect of evanescent waves at the boundaries. This turned out to work well for us, although the structure is not mirror symmetric with respect to the electron axis.

Simulations. The 3D frequency-domain simulation was performed in COMSOL, based on the finite element method. The simulation cell, as shown in the lower right inset of Figure 1c, consists of a single unit cell of the grating, with a height of 4 mm and periodic boundaries along the electron propagation direction. An optional phase shift at the boundaries in longitudinal direction enables simulations for nonperpendicular Smith-Purcell emission, $\lambda \neq a$. Perfectly matched layers are applied in all remaining, transverse directions. The electron beam (E = 3.2 GeV, $Q = e$) had a Gaussian shape of width $\sigma_x = \sigma_z$ = 50 μm in the transverse direction.

The 3D time-domain simulation of the full structure, as shown in Figure 1c with the connecting filaments at the top and bottom, was performed in CST Studio Suite 2021. A single electron bunch (E = 3 GeV) with Gaussian charge distribution was assumed. Its width in the transverse direction was $\sigma_x = \sigma_z$ = 0.1 mm and in the longitudinal direction σ_y = 0.2 mm with cutoff length 0.4 mm. The simulation was performed for a longer bunch length than the experimental bunch length due to computational resource limitations for smaller mesh cell resolutions. Nevertheless, we expect this approximation to yield a realistic emission spectrum, since the simulated bunch length is still substantially shorter than the central wavelength. A convergence test showed that a hexahedral mesh with a minimum cell size of 15 μm was sufficient. To imitate free space, perfectly matched layers and open-space boundary conditions were applied, where a $\lambda/2$ thick layer of vacuum was added after the dielectric structure. The radiation spectrum was then obtained via far-field approximations at multiple frequencies.

Accelerator Setup. The experiments used 10 pC electron bunches from the 3.2 GeV Athos beamline of SwissFEL[27] operated at a pulse repetition rate of 1 Hz to keep particle losses during alignment at a tolerable level. The standard bunch charge at SwissFEL is 200 pC at a repetition rate of 100 Hz. For the low charge working point, the aperture and intensity of the cathode laser are reduced. The normalized emittance of the electron beam with a charge of 9.5 pC was 110 nm rad in both planes and was measured with a quadrupole scan in the injector at a beam energy of 150 MeV.[36]

For the experiment, we scanned the charge from 0 to 11.8 pC by adjusting the intensity of the cathode laser, which results in a slight emittance degradation and mismatch of the transverse beam parameters. This is due to charge density changes in the space charge dominated gun region. Nevertheless, the beam size remained small enough for full transmission through the THz Smith−Purcell structure.

A bunch length of 30 fs (RMS) was measured for similar machine settings in a separate shift with a transverse deflecting cavity (TDC) in the Aramis beamline of the accelerator. Therefore, we expect the longitudinal dimension of the electron beam at the ACHIP chamber to be on the order of 10 μm, almost 2 orders of magnitude shorter than the period of the structure and radiated wavelength.

The transverse beam size at the interaction point was 30 μm in the horizontal and 40 μm in the vertical direction (for a charge of 9.5 pC), as measured with a scintillating YAG screen imaged with an out-of-vacuum microscope onto a CCD camera. After position and angular alignment of the structure using an in-vacuum hexapod, the beam could be transmitted without substantial losses through the 272 μm wide channel of the THz generating structure.

Structure Fabrication. The structure was fabricated with a commercial PMMA stereolithography device Formlabs Form 2. The resolution of the device is 140 μm, which provides subwavelength feature sizes for the geometry with a periodicity of 900 μm. The height of the structure (6 mm) was limited by the stability of the structure rods during the fabrication process. The high temperature resin used for this study can be heated to 235 °C. A sufficiently low outgassing rate for the installation at SwissFEL was achieved after baking the device for 5 h under vacuum conditions at 175 °C.[24] Thanks to the rapid improvements in SLA technology and other free-form manufacturing techniques, the geometry could certainly be fabricated also at shorter wavelengths and higher resolution for future experiments. An increased manufacturing quality is required to achieve an even narrower emission bandwidth.

Michelson Interferometer and THz Detector. For the spectrum measurements, we installed a Michelson interfer-

https://doi.org/10.1021/acsphotonics.1c01932
ACS Photonics 2022, 9, 1143−1149

ometer outside the vacuum chamber. The THz pulse was first sent through an in-vacuum lens made of PMMA with a diameter of 25 mm and a focal length of 100 mm. The lens collimates radiation in the vertical plane, but it does not map the entire radiation of the 45 mm long structure onto the detector. The angular acceptance in the horizontal plane is calculated via ray tracing (see Figure 3). A fused silica vacuum window with about 50% transmission for the design wavelength of the structure (900 μm) is used as extraction port.

The beam splitter is made of 3.5 mm-thick plano−plano high-resistivity float-zone silicon (HRFZ-Si) manufactured by TYDEX. It provides a splitting ratio of 54/46 for wavelengths ranging from 0.1 to 1 mm. Translating one of the mirrors of the interferometer allowed us to measure the first-order autocorrelation, from which the power spectrum is obtained via Fourier transform.

The geometric acceptance angle of the Michelson interferometer $\Delta\theta$ in the plane of the electron beam and the THz radiation defines the accepted bandwidth of the setup. According to the Smith−Purcell relation (eq 1), it is given by

$$\Delta\lambda = a \sin\theta\Delta\theta$$

Around the orthogonal direction (θ = 90°), the accepted bandwidth covers the measured spectrum (Figure 3). We calculated the acceptance with ray tracing including the size of the emitting structure and the apertures of the collimating lens (25 mm) and the detector (12 mm).

A Schottky diode (ACST, Type 3DL 12C LS2500 A2) was used as THz detector, sensitive from 300 to 4000 μm. The manufacturer indicates a responsivity of 120 V/W at 900 μm, which we used to estimate the energy deposited on the detector. The signal from the detector is transmitted via a 20 m long coaxial cable to an oscilloscope outside of the accelerator bunker. For absolute pulse energy measurements, the detector setup including absorption in cables and the vacuum window should be characterized with a calibrated THz source. We calculated the pulse energy for different charges (Figure 4) by averaging over all shots during the oscillating autocorrelation measurement.

A typical autocorrelation measurement for a charge of 9.4 pC is depicted in Figure 2b. The shape of the autocorrelation is not perfectly symmetric in amplitude and stage position. The amplitude asymmetry could be a result of a nonlinear detector response (onset of saturation). This is in agreement with the slight deviation of the pulse energy from the quadratic fit (Figure 4). Since the length of only one arm is changed and the radiation might not be perfectly collimated, the position scan of the mirror is not creating a perfectly symmetric autocorrelation signal.

AUTHOR INFORMATION

Corresponding Author

Rasmus Ischebeck − *Paul Scherrer Institut, 5232 Villigen, PSI, Switzerland;* orcid.org/0000-0002-5612-5828; Email: rasmus.ischebeck@psi.ch

Authors

Benedikt Hermann − *Paul Scherrer Institut, 5232 Villigen, PSI, Switzerland; Institute of Applied Physics, University of Bern, 3012 Bern, Switzerland; Galatea Laboratory, Ecole Polytechnique Fédérale de Lausanne (EPFL), 2000 Neuchâtel, Switzerland;* orcid.org/0000-0001-9766-3270

Urs Haeusler − *Department Physik, Friedrich-Alexander-Universität Erlangen-Nürnberg (FAU), 91058 Erlangen, Germany; Cavendish Laboratory, University of Cambridge, Cambridge CB3 0HE, United Kingdom;* orcid.org/0000-0002-6818-0576

Gyanendra Yadav − *Department of Physics, University of Liverpool, Liverpool L69 7ZE, United Kingdom; Cockcroft Institute, Warrington WA4 4AD, United Kingdom*

Adrian Kirchner − *Department Physik, Friedrich-Alexander-Universität Erlangen-Nürnberg (FAU), 91058 Erlangen, Germany*

Thomas Feurer − *Institute of Applied Physics, University of Bern, 3012 Bern, Switzerland*

Carsten Welsch − *Department of Physics, University of Liverpool, Liverpool L69 7ZE, United Kingdom; Cockcroft Institute, Warrington WA4 4AD, United Kingdom*

Peter Hommelhoff − *Department Physik, Friedrich-Alexander-Universität Erlangen-Nürnberg (FAU), 91058 Erlangen, Germany*

Complete contact information is available at: https://pubs.acs.org/10.1021/acsphotonics.1c01932

Author Contributions

[#]These authors contributed equally to this work. B.H., U.H., P.H., and R.I. conceived the project. U.H. optimized the design. B.H. fabricated the structure and performed the experiments with support from R.I. and A.K. Simulations in CST were performed by G.Y. All authors discussed the results and contributed to the manuscript.

Funding

Gordon and Betty Moore Foundation (4744, "ACHIP") and ERC Advanced Grant (884217, "AccelOnChip").

Notes

The authors declare no competing financial interest.

ACKNOWLEDGMENTS

We thank the SwissFEL operations crew, the expert groups at PSI, and the entire ACHIP collaboration for their support. We thank Thomas Schietinger for careful proofreading. Data underlying the results presented in this paper are not publicly available at this time but may be obtained from the authors upon reasonable request.

REFERENCES

(1) Seeds, A. J.; Shams, H.; Fice, M. J.; Renaud, C. C. Terahertz photonics for wireless communications. *J. Lightwave Technol.* **2015**, *33*, 579−587.

(2) Hafez, H. A.; et al. Intense terahertz radiation and their applications. *J. Opt.* **2016**, *18*, 093004.

(3) Nanni, E. A.; Huang, W. R.; Hong, K.-H.; Ravi, K.; Fallahi, A.; Moriena, G.; Dwayne Miller, R. J.; Kartner, F. X. Terahertz-driven linear electron acceleration. *Nat. Commun.* **2015**, *6*, 1−8.

(4) Hibberd, M. T.; et al. Acceleration of relativistic beams using laser-generated terahertz pulses. *Nat. Photonics* **2020**, *14*, 755−759.

(5) Xu, H.; et al. Cascaded high-gradient terahertz-driven acceleration of relativistic electron beams. *Nat. Photonics* **2021**, *15*, 426−430.

(6) Tanaka, K.; Hirori, H.; Nagai, M. THz nonlinear spectroscopy of solids. *IEEE Trans. Terahertz Sci. Technol.* **2011**, *1*, 301−312.

(7) Son, J.-H. *Terahertz Biomedical Science and Technology*; CRC Press, 2014.

(8) Schneidmiller, E. A.; Yurkov, M. V.; Krasilnikov, M.; Stephan, F. In *Tunable IR/THz Source for Pump Probe Experiments at the European XFEL*; Tschentscher, T., Tiedtke, K., Eds.; Advances in X-ray Free-

Electron Lasers II: Instrumentation, International Society for Optics and Photonics, SPIE, 2013; Vol. *8778*, pp 151−156.
(9) Zhang, X.; Jin, Y.; Ma, X. F. Coherent measurement of THz optical rectification from electro-optic crystals. *Appl. Phys. Lett.* **1992**, *61*, 2764−2766.
(10) Fülöp, J. A.; et al. Generation of sub-mj terahertz pulses by optical rectification. *Opt. Lett.* **2012**, *37*, 557−559.
(11) Smith, S. J.; Purcell, E. M. Visible light from localized surface charges moving across a grating. *Phys. Rev.* **1953**, *92*, 1069−1069.
(12) Doucas, G.; Mulvey, J. H.; Omori, M.; Walsh, J.; Kimmitt, M. F. First observation of Smith-Purcell radiation from relativistic electrons. *Phys. Rev. Lett.* **1992**, *69*, 1761−1764.
(13) Kube, G.; et al. Observation of optical Smith-Purcell radiation at an electron beam energy of 855 MeV. *Phys. Rev. E* **2002**, *65*, 056501.
(14) Ishi, K.; et al. Observation of coherent smith-purcell radiation from short-bunched electrons. *Phys. Rev. E* **1995**, *51*, R5212−R5215.
(15) Brownell, J. H.; et al. The angular distribution of the power produced by Smith-Purcell radiation. *J. Phys. D: Appl. Phys.* **1997**, *30*, 2478−2481.
(16) Rusin, F.; Bogomolov, G. Orotron—an electronic oscillator with an open resonator and reflecting grating. *Proc. IEEE* **1969**, *57*, 720−722.
(17) Zhang, P.; Ang, L. K.; Gover, A. Enhancement of coherent smith-purcell radiation at terahertz frequency by optimized grating, prebunched beams, and open cavity. *Phys. Rev. ST Accel. Beams* **2015**, *18*, 020702.
(18) England, R. J.; et al. Dielectric laser accelerators. *Rev. Mod. Phys.* **2014**, *86*, 1337.
(19) Molesky, S.; et al. Inverse design in nanophotonics. *Nat. Photonics* **2018**, *12*, 659−670.
(20) Su, L.; Piggott, A. Y.; Sapra, N. V.; Petykiewicz, J.; Vučković, J. Inverse design and demonstration of a compact on-chip narrowband three-channel wavelength demultiplexer. *ACS Photonics* **2018**, *5*, 301−305.
(21) Su, L.; et al. Fully-automated optimization of grating couplers. *Opt. Express* **2018**, *26*, 4023−4034.
(22) Sapra, N. V.; et al. On-chip integrated laser-driven particle accelerator. *Science* **2020**, *367*, 79−83.
(23) Szczepkowicz, A.; Schächter, L.; England, R. J. Frequency-domain calculation of smith−purcell radiation for metallic and dielectric gratings. *Appl. Opt.* **2020**, *59*, 11146−11155.
(24) Kellermeier, M.; et al. Towards additive manufacturing of dielectric accelerating structures. *J. Phys.: Conf. Ser.* **2020**, *1596*, 012020.
(25) Kingma, D. P.; Ba, J. Adam: A method for stochastic optimization. *3rd International Conference on Learning Representations*; ICLR, 2015; Vols. *1−15*.
(26) Ferrari, E.; et al. The ACHIP experimental chambers at the Paul Scherrer Institut. *Nucl. Instrum. Methods Phys. Res., Sect. A* **2018**, *907*, 244−247.
(27) Milne, C. J.; et al. SwissFEL: The Swiss X-ray free electron laser. *Appl. Sci.* **2017**, *7*, 720.
(28) Kampfrath, T.; Tanaka, K.; Nelson, K. A. Resonant and nonresonant control over matter and light by intense terahertz transients. *Nat. Photonics* **2013**, *7*, 680−690.
(29) Nicoletti, D.; Cavalleri, A. Nonlinear light−matter interaction at terahertz frequencies. *Adv. Opt. Photonics* **2016**, *8*, 401−464.
(30) Roques-Carmes, C.; Kooi, S. E.; Yang, Y.; Massuda, A.; Keathley, P. D.; Zaidi, A.; Yang, Y.; Joannopoulos, J. D.; Berggren, K. K.; Kaminer, I.; Soljacic, M. Towards integrated tunable all-silicon free-electron light sources. *Nat. Commun.* **2019**, *10*, 1−8.
(31) Ye, Y.; et al. Deep-ultraviolet smith−purcell radiation. *Optica* **2019**, *6*, 592−597.
(32) Hughes, T. W.; Williamson, I. A.; Minkov, M.; Fan, S. Forward-mode differentiation of Maxwell's Equations. *ACS Photonics* **2019**, *6*, 3010−3016.
(33) Hughes, T.; Veronis, G.; Wootton, K. P.; England, R. J.; Fan, S. Method for computationally efficient design of dielectric laser accelerator structures. *Opt. Express* **2017**, *25*, 15414−15427.
(34) Van den Berg, P. Smith−purcell radiation from a line charge moving parallel to a reflection grating. *J. Opt. Soc. Am.* **1973**, *63*, 689−698.
(35) Fang, J.; Wu, Z. Generalized perfectly matched layer for the absorption of propagating and evanescent waves in lossless and lossy media. *IEEE Trans. Microwave Theory Technol.* **1996**, *44*, 2216−2222.
(36) Prat, E. Symmetric single-quadrupole-magnet scan method to measure the 2d transverse beam parameters. *Nucl. Instrum. Methods Phys. Res., Sect. A* **2014**, *743*, 103−108.

https://doi.org/10.1021/acsphotonics.1c01932
ACS Photonics 2022, 9, 1143−1149